

Analysis of Navier-Stokes Codes Applied to Supersonic Retro-Propulsion Wind Tunnel Test

Kerry A. Trumble (Kerry.A.Trumble@NASA.gov, 650-604-4973)
NASA Ames Research Center, Moffett Field, CA 94035

Daniel G. Schauerhamer (Daniel.G.Schauerhamer@NASA.gov, 281-483-0528)
Jacobs Technology, Houston, TX 77058

William L. Kleb, (Bil.Kleb@NASA.gov, 757-864-4364)
Jan-Renee Carlson (Jan-Renee.Carlson@NASA.gov, 757-864-3047)
Karl T. Edquist (Karl.T.Edquist@NASA.gov, 757-864-4566)
NASA Langley Research Center, Hampton, VA 23681

Abstract—This paper describes the pre-test analysis of three Navier-Stokes codes applied to a Supersonic Retro-Propulsion (SRP) wind tunnel test.^{1,2} Advancement of SRP as a technology hinges partially on the ability of computational methods to accurately predict vehicle aerodynamics during the SRP phase of atmospheric descent. A wind tunnel test at the Langley Unitary Plan Wind Tunnel was specifically designed to validate Navier-Stokes codes for SRP applications. The test consisted of a 5-inch diameter, 70-degree sphere-cone forebody with cylindrical afterbody, with four configurations spanning 0 to 4 jets. Test data include surface pressure (including high-frequency response), flowfield imagery, and internal pressure and temperature measurements. Three computational fluid dynamics (CFD) codes (DPLR, FUN3D, and OVERFLOW) are exercised for both single and multiple-nozzle configurations for a range of Mach (M) numbers and thrust coefficients. Comparisons to test data will be used to evaluate accuracy, identify modeling shortcomings, and gain insight into the computational requirements necessary for computing these complex flows.

TABLE OF CONTENTS

1. INTRODUCTION	1
2. COMPUTATIONAL METHODS	2
3. WIND TUNNEL MODEL DESIGN	3
4. PRE-TEST CFD ANALYSIS	5
5. SUMMARY	11
REFERENCES	12

1. INTRODUCTION

Supersonic Retro-Propulsion has been proposed as a means to decelerate Exploration-scale missions (10s of metric tons) to the surface of Mars. [1] Aerodynamics is important for predicting vehicle stability and controllability, and aeroheating determines thermal protection requirements. The advancement of SRP as a technology will be strongly influenced by the advancement of computational fluid

dynamics to predict aerodynamics and aeroheating during the SRP phase of atmospheric descent.

SRP is envisioned as a replacement for supersonic parachutes by initiating propulsive descent at supersonic Mach numbers with the engines directed into the oncoming freestream, a deceleration technique that has never been demonstrated. [2] Parachute decelerators that have previously been used for robotic Mars missions (less than one metric ton payload) have poor scalability with increasing payload mass. It is expected that the SRP system will not only increase the total effective vehicle drag and aid attitude control during descent, but it will also cause additional forces and moments due to the interaction of the exhaust plumes and freestream.

Preliminary CFD assessment and development has been leveraged from existing SRP fluid dynamics knowledge base that consists primarily of an unrelated series of wind tunnel tests on blunt bodies during the Apollo and Viking eras. [3,4] These wind tunnel tests are incomplete and have many inconsistencies, and typically are not detailed enough for useful CFD analysis. For instance, static conditions are recorded but dynamics of the interactions between the freestream and the plume are not mentioned at all. In light of these shortcomings, it was determined that new wind tunnel experiments are required to provide higher fidelity data for CFD validation exercises that demonstrate modeling strengths and weaknesses. The current experiment is designed specifically to qualitatively and quantitatively determine the capability of the CFD codes DPLR [5], FUN3D [6,7] and OVERFLOW [8] to characterize supersonic retro-propulsion physical phenomenon.

Jarvinen and Adams [9] described the characteristics of a single SRP jet flowfield in Figure 1. The principal parameter that characterizes the interaction of the jet plume with the opposing freestream is the *thrust coefficient* ($C_T = T/q_\infty A_B$), where T is the thrust, q_∞ is the freestream dynamic pressure, and A_B is the reference area. The complex interaction between the jet plume and external flowfield is expected to stress the capabilities of existing

¹ 978-1-4244-7351-9/11/\$26.00 ©2011 IEEE

² IEEEAC paper#1471, Version 1, Updated 2010:10:26

CFD codes and will drive further development in numerous areas, including grid generation/adaption and turbulence modeling. [3] The three codes are being tested for both single and multiple-nozzle configurations for a range of Mach numbers and thrust coefficients. Quantitative (surface pressure, forces and moments) and qualitative (flowfield structure) comparisons will be used to evaluate the codes and identify modeling capabilities. The present paper will discuss the model design process for the Langley UPWT experiment, including the influence of pre-test CFD on model diameter and radial location of periphery nozzles. The paper will also discuss the pre-test CFD analysis to determine the effects, if any, of the tunnel wall interference and possible liquefaction within the plumes. For further discussion on the design of the experiment, please refer to the paper by Berry et al. [10]

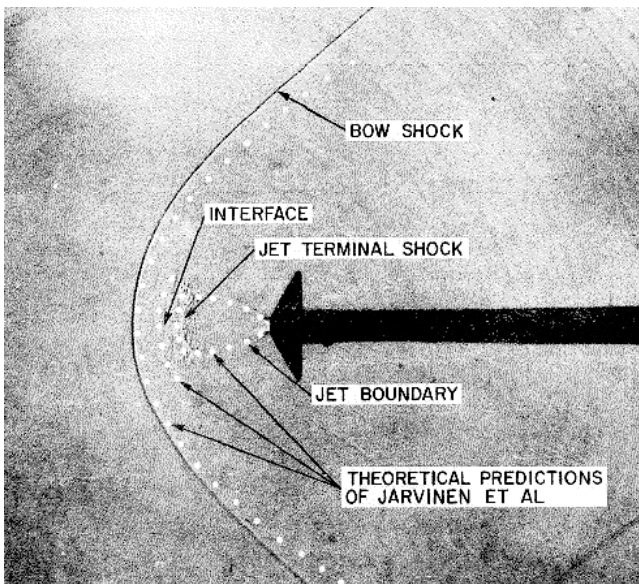


Figure 1: SRP jet plume characteristics described by Jarvinen and Adams for a 60-degree sphere-cone in freestream Mach 2 and $C_T=1.0$. [9]

2. COMPUTATIONAL METHODS

CFD is a valuable means of determining important design factors such as aerodynamics and aerothermodynamics. These analyses are then leveraged to design vehicle systems such as guidance, navigation and control (GN&C) and thermal protection systems on full-scale vehicles. It is important that the CFD tool's capabilities are well understood. Three different CFD codes utilizing finite-volume or finite-difference methods are employed to assess their respective capabilities for simulating SRP flows: cell-centered structured grid, node-centered overset structured grid, and node-centered unstructured grid. All codes assume perfect gas in the presented results. DPLR and OVERFLOW modeled a full 3D geometry. FUN3D modeled half geometry with a symmetry plane. A brief summary of each code is given below.

DPLR

The Data Parallel Line Relaxation (DPLR) CFD code [5] is a parallel, structured multi-block, finite-volume code that solves the Navier-Stokes equations for continuum flow, including finite-rate chemistry and thermal non-equilibrium. In the present study the equations are solved implicitly in time with first-order accuracy, although DPLR can be run second-order time implicit with sub-iterations. Euler fluxes are computed using modified Steger-Warming flux vector splitting [11] with third-order spatial accuracy via MUSCL extrapolation with a minmod limiter. [12] The viscous fluxes are computed with second-order spatial accuracy using a central difference approach. For the present analysis, the Shear-Stress Transport (SST) turbulence model was employed with a vorticity-based production term. Although DPLR includes overset grid capabilities, the presented results are with point-matched grid systems.

FUN3D

The Fully Unstructured Navier-Stokes Three-Dimensional suite of codes (FUN3D) contains a node-based finite-volume flow solver. [6,7] The FUN3D website, <http://fun3d.larc.nasa.gov>, contains the user manual and an extensive list of references. FUN3D can solve unsteady, incompressible and compressible, Euler and Navier-Stokes flow with thermochemical non-equilibrium. The present study employs Edwards' Low Diffusion Flux-Splitting Scheme (LDFSS) [13] with a Van Albada limiter [14] to solve the compressible Reynolds-Averaged Navier-Stokes (RANS) equations coupled to Menter's SST turbulence model. The SST model here is strain-based. All node-based conservative variables are computed by driving a second-order accurate spatial residual to steady-state with a point-implicit iterative method. For steady flows, local time stepping is employed and for unsteady flows, up to fourth-order time accuracy is available via sub-iterations. FUN3D can utilize general mixed-element grids and overset grid systems, but only tetrahedral grids are used in this study. Automatic domain decomposition is employed to fully exploit distributed memory and by using the parallel grid adaptation mechanics by Park and Darmofal, Mach Hessian gradient-based adaptation was used to sharpen flow features. [15,16]

OVERFLOW

OVERFLOW 2 [8] is an implicit RANS flow solver that utilizes structured overset grids. [17,18] Several Euler flux schemes are available, including central differencing and a number of upwind schemes. [19,20] Implicit time advance schemes include block tri-diagonal Alternating Direction Implicit (ADI), scalar pentadiagonal ADI [21] and Symmetric Successive Over-Relaxation method (SSOR). Newton sub-iteration or dual time stepping can be used for second-order, time-accurate simulations. [22,23] Turbulence models include Baldwin-Barth [24], Spalart-Allmaras [25], and SST [26]. Other OVERFLOW capabilities include automatic domain decomposition and partitioning for

parallel processing [27,28], automatic off-body grid generation with adaptation [29,30], grid sequencing and multigrid, low-Mach preconditioning, a full six-degree-of-freedom solver with collision detection [31,32], and the ability to solve applications with multiple species. For the current work, the numerical flux function HLLC++ (Harten, Lax, van Leer, and Einfeldt) with the Van Albada limiter was used for spatial terms, and the SSOR algorithm with dual time stepping using Newton sub-iterations for temporal terms. All viscous terms were included, and the strain-based SST turbulence model was employed. The overall scheme is second-order accurate in space and time. The inviscid flux calculations for both the flow solver and the turbulence model use third-order accurate MUSCL extrapolation.

3. WIND TUNNEL MODEL DESIGN

The Langley Unitary Plan Wind Tunnel (4-foot by 4-foot test section) was chosen for its relatively large test section and relevant Mach number range (2.4 to 4.6 in test section 2). The model was initially chosen to be a 70-degree sphere-cone with a 6-inch diameter and a cylindrical afterbody. The thought was that a 6-inch model would have sufficient internal volume for the air distribution system and instrumentation. The nozzle configuration would allow for zero-nozzle, single-nozzle at center of model, two three-nozzle configurations at different radial locations on the periphery of the model, and two four-nozzle configurations, which include the center nozzle and either of the three peripheral configurations (Figure 2). The three peripheral nozzles would be at the $\frac{1}{2}$ and $\frac{3}{4}$ radial locations. The rays through the center of the model to the shoulder will be characterized with phi (ϕ), where 0-degree intersects at the top of the model and 90-degree is at the right (Figure 16). The experiment design was aided by CFD to refine the model scale, determine effects of tunnel walls, and assess the nozzle configurations.

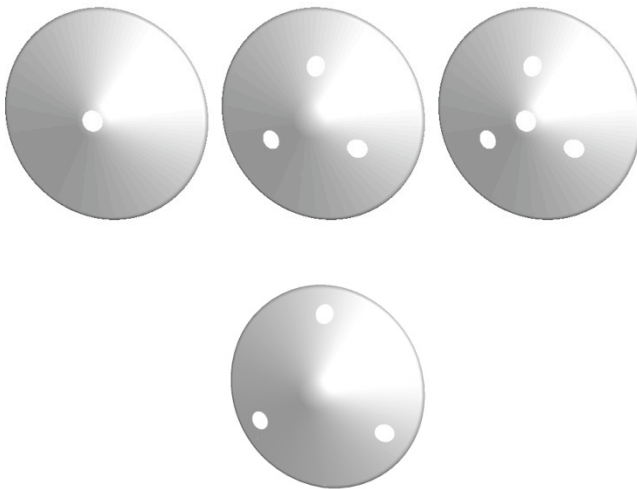


Figure 2: Initial nozzle configurations: single (left), three at 1/2 radial location (middle top) and at 3/4 radial location (middle bottom), and four (right).

The CFD assessment case matrix included freestream Mach numbers of 2.4, 3.5, and 4.6, thrust coefficients of 0, 5, and 10, and angles-of-attack of 0, 5, and 10 degrees. During the initial assessment, only the single-nozzle and both three-nozzle configurations were analyzed.

The model diameter and allowable thrust coefficient both influence whether or not the tunnel walls can affect the pressures seen by the model; and for more extreme cases, whether the tunnel would be blocked, causing it to unstart or contaminate the freestream. Initial results for the 6-inch diameter model with the three-nozzle configuration at the $\frac{3}{4}$ radial location suggest that the walls would influence the surface quantities and possibly even unstart the tunnel (large region of subsonic flow). Given that the wind tunnel test was designed for CFD validation, having to include tunnel walls in the flowfield simulations was considered to be an unnecessary complication and not relevant to flight conditions. To investigate wall effects a 4-inch diameter model was also analyzed.

Figure 3 shows FUN3D solutions that demonstrate the effect of tunnel walls, modeled inviscidly, on surface pressure distributions. The plots are differences in surface pressure between a simulation with and without tunnel walls for a thrust coefficient of 10, Mach 4.6, 3.5, and 2.4, and angle-of-attack 0, 5, and 10 degrees. In the plot, the white sections signify no difference between the simulations, indicating no influence from the tunnel walls. The large red and some blue pockets are noted, which show at least a 1 psi difference between simulations with and without walls. For these cases, modeling of the tunnel walls would be necessary in the CFD modeling, an unnecessary complication for validation exercises.

DPLR and OVERFLOW were used on a subset of these cases including an overlapping case for all codes (Figure 4). FUN3D and OVERFLOW are in agreement on the general flowfield structure and both codes predicted relatively steady plumes. The plume predicted by DPLR was unsteady. FUN3D was run with local time stepping, while DPLR and OVERFLOW solutions were advanced using a global time stepping approach.

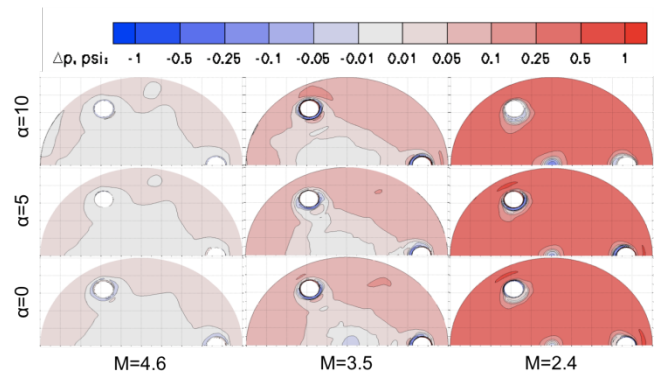


Figure 3: Subset of FUN3D solutions for pre-test wind tunnel model design at Mach 4.6, 3.5, and 2.4 and

angles-of-attack of 10, 5, and 0 degrees for a thrust coefficient of 10. Contours are surface pressure differences between solutions with and without tunnel walls

From the large database of CFD cases, it was seen that tunnel wall effects increased with higher thrust coefficients, lower Mach numbers, and with the larger model diameter. Also, the 6-inch diameter model at high thrust coefficients and low Mach numbers became a candidate to cause tunnel blockage (Figure 5) that could potentially damage the model instrumentation. A 4-inch model was shown to be the better choice to minimize tunnel effects. However, this model was too small for packaging the internal instrumentation, so a 5-inch diameter model was chosen as a compromise. The reduction in model diameter also resulted in the removal of the 3/4 radial peripheral nozzles due to internal packaging limitations.

The CFD temperatures within the plume were predicted to be as low as 10 K, well below the liquefaction temperature for air. In order to avoid the need to model two-phase flow, which would be out of the scope of this CFD validation experiment, the nozzle area ratio was lowered from 9 to 4 and the nozzle gas in the plenum would be heated as high as possible to avoid liquefaction. The internal flow path in the plenum and fingers was simulated with FUN3D. The solution indicated flow separation downstream of the feed lines to the 3/4 radial peripheral nozzles (Figure 6). In this simulation, the other nozzles are plugged and therefore contain no flow. In order to avoid separation, the internal corners within the flow path were smoothed and, as mentioned earlier, the 3/4 radial peripheral nozzles were removed.

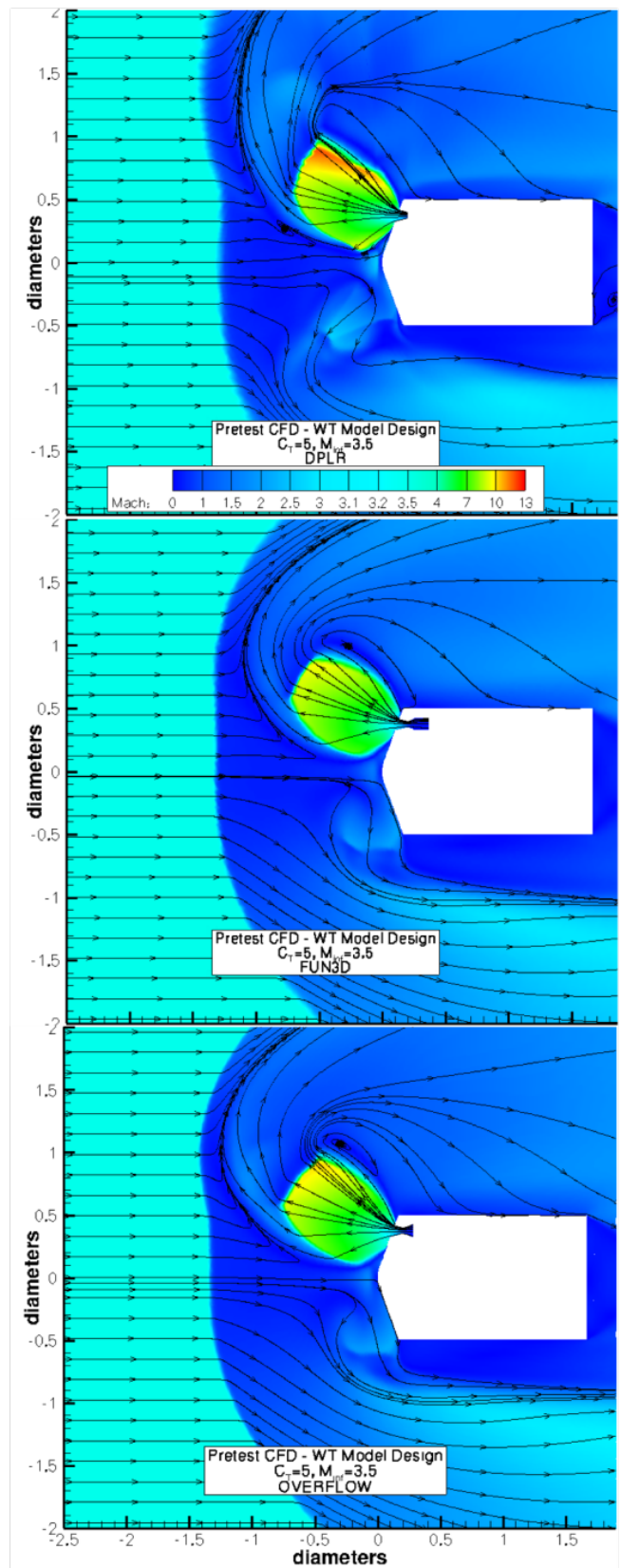


Figure 4: Mach contours for 6-inch diameter, 3/4 radial periphery configuration wind tunnel model design at $M_\infty=3.5$ and $C_1=5$ for DPLR (top), FUN3D (middle) and OVERFLOW (bottom).

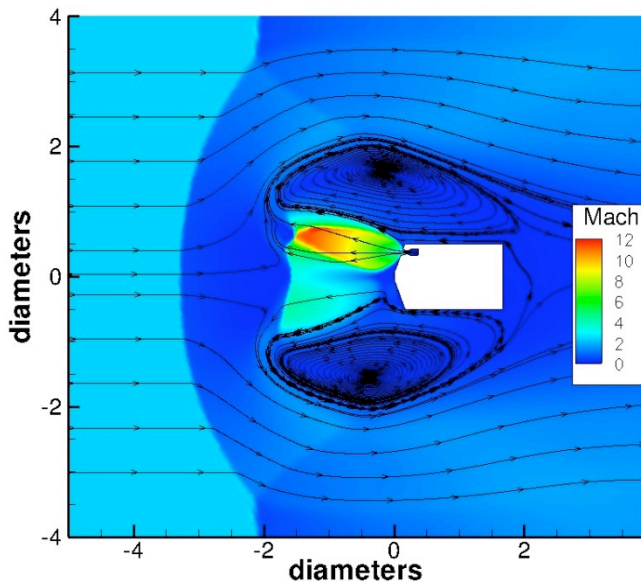


Figure 5: Potential tunnel blockage due to a 6-inch diameter model at $M=2.4$ and $C_T=10$ as predicted with FUN3D. The bounds on the y-axis are the locations of the tunnel walls, modeled inviscidly.

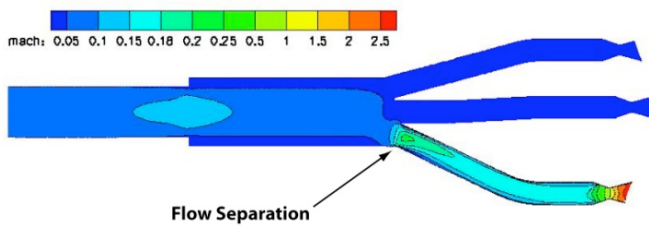


Figure 6: Mach contours on the symmetry plane from an internal solution for an early plenum and nozzle design with seven fingers.

4. PRE-TEST CFD ANALYSIS

Once the model dimensions and nozzle configuration were chosen (Figure 7), a matrix of pre-test CFD cases was run in order to identify expected outcomes from the wind tunnel experiment and also to assess code-to-code comparisons. The pre-test CFD matrix is shown in Table 1. The test section was assumed symmetric and the tunnel walls were modeled inviscidly. The inviscid assumption is non-conservative based on FUN3D calculations. A preliminary assessment of the tunnel boundary layer was performed with FUN3D by modeling the settling chamber, nozzle, and test section of the tunnel geometry with viscous walls at Mach 2.4. The FUN3D test section flowfield (Figure 8) indicates that the desired freestream Mach of 2.4 is within 6% compared to calibration data, however the boundary layer is thick and comprises nearly one-third of the tunnel test section.



Figure 7: Final model design mounted in the tunnel. The zero-nozzle configuration is shown.

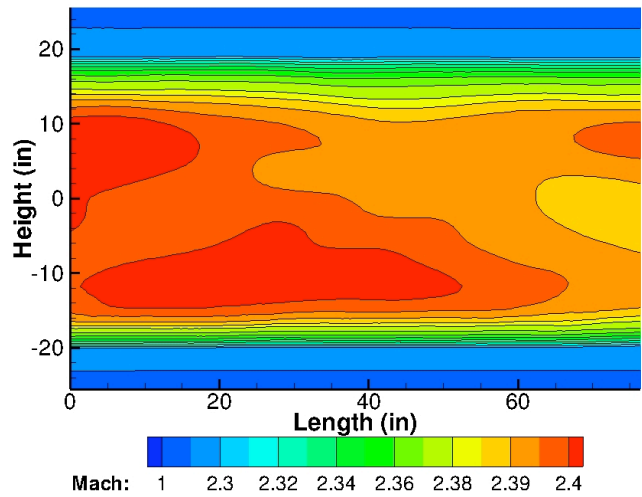


Figure 8: Wind tunnel test section Mach contours which illustrates the thickness of the boundary layer at the walls.

Priority	Nozzles	AOA (deg)	Mach	CT
1	0	0, 2, 10	2.4	0
2			3.5	0
3			4.6	0
4	1	0	2.4	5
5			10	
6	1	0	4.6	5
7			10	
8	1	10	2.4	5
9			10	
10	1	10	4.6	5
11			10	
12	3	0	2.4	5
13			10	
14	3	0	4.6	5
15			10	
16	4	0	2.4	5
17			10	
18	4	0	4.6	5
19			10	
20	4	10	2.4	5
21			10	
22	4	10	4.6	5
23			10	
24	1	2	2.4	5
25			10	
26	1	2	4.6	5
27			10	
28	4	2	2.4	5
29			10	
30	4	2	4.6	5
31			10	

Table 1: Pre-test CFD case matrix, prioritizing number of nozzles, angle-of-attack, freestream Mach number, and thrust coefficient.

Zero-Nozzle Configuration

As expected, good agreement between the codes is seen in the zero-nozzle configuration. This configuration is the well-understood supersonic blunt body flow. Bow shock stand-off distances are in agreement within the codes (Figure 9). The surface pressure coefficients are in agreement on the flank region of the model, but differ the most at the nose (Figure 10). For example, there is up to 4% disagreement on the nose for the case at $M=4.6$ and $\alpha=0$ -degree, which could be carbuncle effects at the stagnation point. As a reference, the theoretical normal shock pressure coefficient at the stagnation point is shown as the black symbols in the figure for $\alpha=0$ -degree.

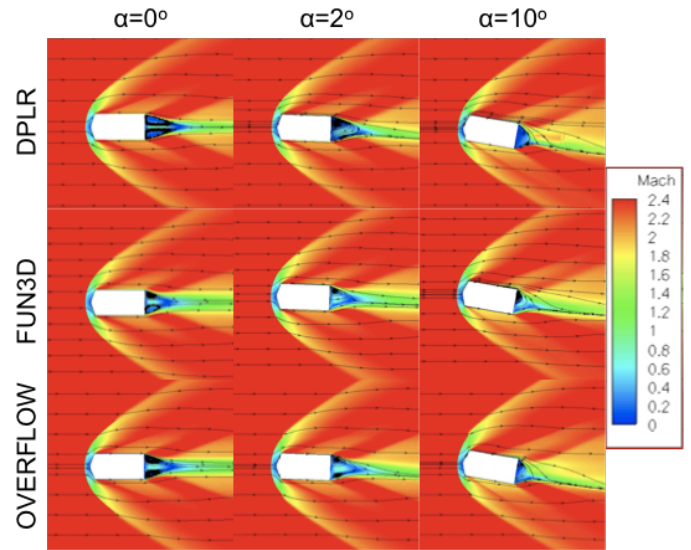


Figure 9: Zero-nozzle configuration Mach contours at 0, 2, and 10 degrees angles-of-attack at $M=2.4$ for DPLR (top), FUN3D (middle), and OVERFLOW (bottom).

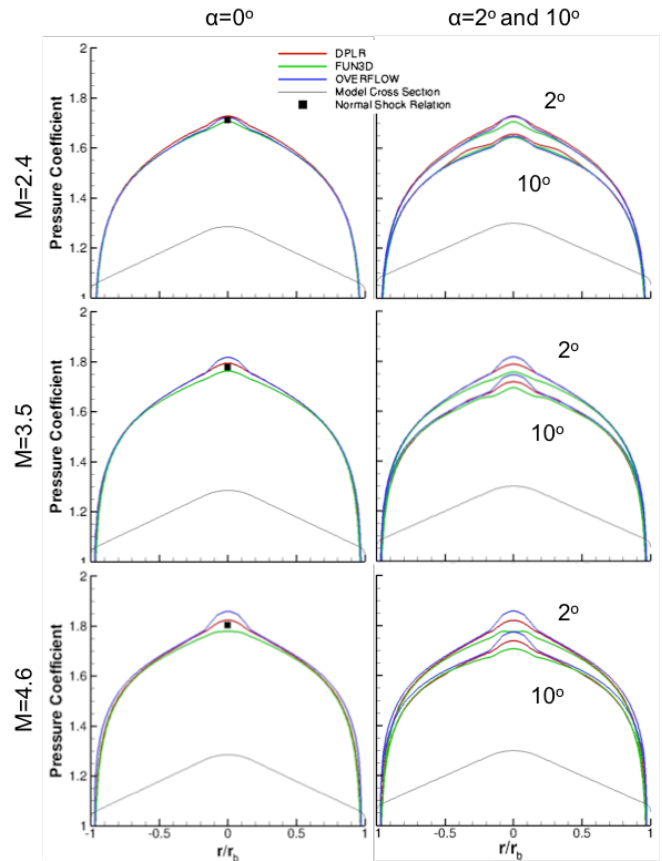


Figure 10: Pressure coefficient slices at $\phi=90^\circ$ for zero-nozzle configuration model for DPLR (red), FUN3D (green), OVERFLOW (blue) and normal shock properties (black square). The model cross section is shown as a black line.

Single-Nozzle

For this configuration, a single nozzle is located at the center of the model. CFD solutions indicate that the largest amount of tunnel interference is shown at $M=2.4$, $C_T=10$, $\alpha=0$ -degree (Figure 11). At this test condition, Mach reflection off the wall occurs about one diameter ahead of the model forebody. In contrast, at this same Mach number and $C_T=5$ the Mach reflection occurs two diameters downstream of the model forebody.

The three codes are in good agreement with bow shock, termination shock and interface locations (Table 2). The largest percent difference at $\alpha=0$ -degree in bow shock location is 9.5% for $M=2.4$, $C_T=10$, and 9% in termination shock location for $M=4.6$, $C_T=5$. The codes differ, however, in that DPLR predicts unsteadiness at the triple point, which is defined as the location where the shear layer from the plume, the termination shock, and the recirculation region meet. It could also be described as the corners of the plume. FUN3D consistently predicts steady flows. OVERFLOW predicts both steady and unsteady. All results presented here are instantaneous, regardless of the steadiness of the solution.

Pressure coefficients (Figure 12) are in agreement for most of the single-nozzle cases. In the $M=2.4$, $C_T=10$ case the DPLR solution has a lower expansion ratio in the plume. The recirculation region is centered above the model, rather than behind as with FUN3D and OVERFLOW. The subsequent pressure coefficient on the model surface for DPLR is much higher than FUN3D and OVERFLOW by as much as 92%. The difference between FUN3D and OVERFLOW is about 28%. The discrepancy in expansion ratio and pressure coefficient is isolated to this particular run and is not seen in any of the other cases.

The effects of angle-of-attack on the Mach reflections for $M=2.4$ and $C_T=5$ and 10 are shown in Figure 13. For brevity only FUN3D solutions are shown. The same trends are held for the other two codes. As the angle-of-attack is increased the Mach reflection on the lower wall is pushed back by about $\frac{1}{2}$ diameter from 0-degree to 10-degree for both thrust coefficients. The Mach reflection on the upper wall, conversely, is moved $\frac{1}{2}$ diameter upstream. However, the change in Mach reflection location is greater between thrust coefficients than angles-of-attack. For $M=2.4$ the Mach reflection is moved upstream 2 diameters when going from $C_T=5$ to $C_T=10$. The effects of angle-of-attack on pressure coefficient are shown in Figure 14. Again, only FUN3D solutions are shown for simplicity. The differences in pressure coefficient between 0-degree to 2-degree are minimal, an asymmetry develops but the levels remain the same. At 10-degree the pressure coefficient is increased significantly at $C_T=5$ due to the oncoming flow having a direct path to the face of the model. The pressure coefficient at $C_T=10$ is lowered due to greater separation on the face caused by the larger plume.

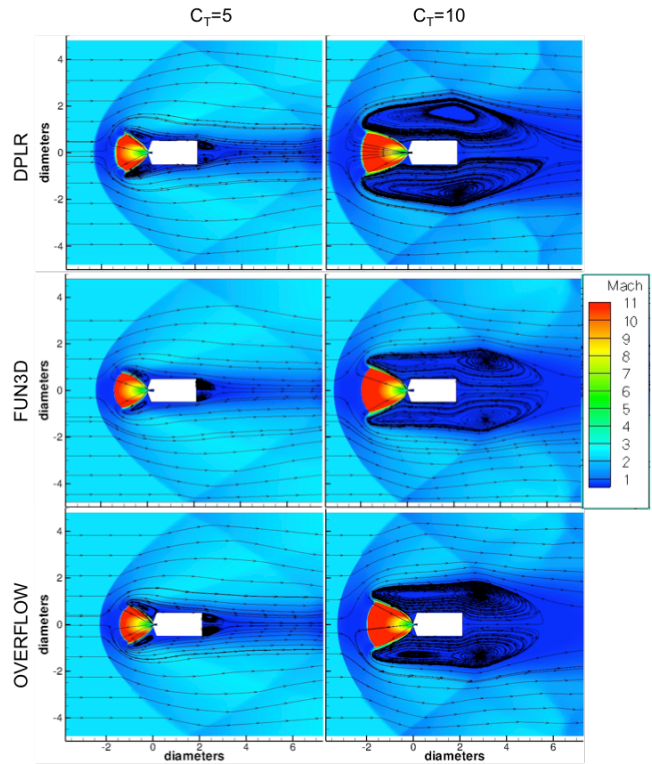


Figure 11: Mach contours for single-nozzle configuration at $M=2.4$, $C_T=5$ and 10 for DPLR (top), FUN3D (middle), and OVERFLOW (bottom).

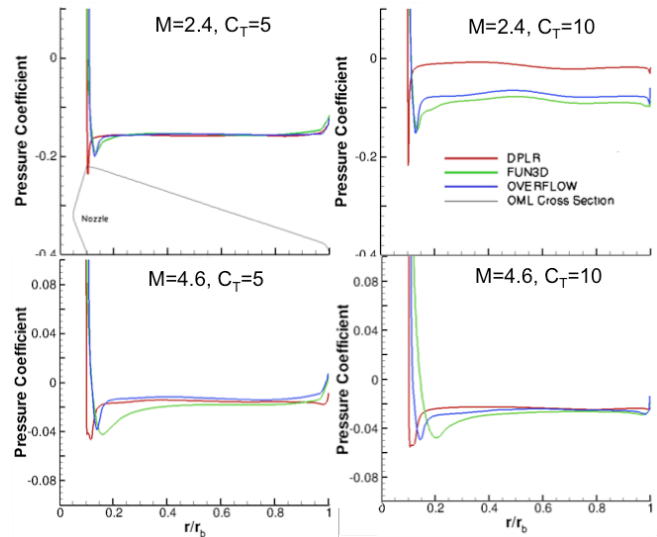


Figure 12: Pressure coefficient slices for single-nozzle configuration at $M=2.4$ and 4.6, $C_T=5$ and 10 for DPLR (red), FUN3D (green), OVERFLOW (blue).

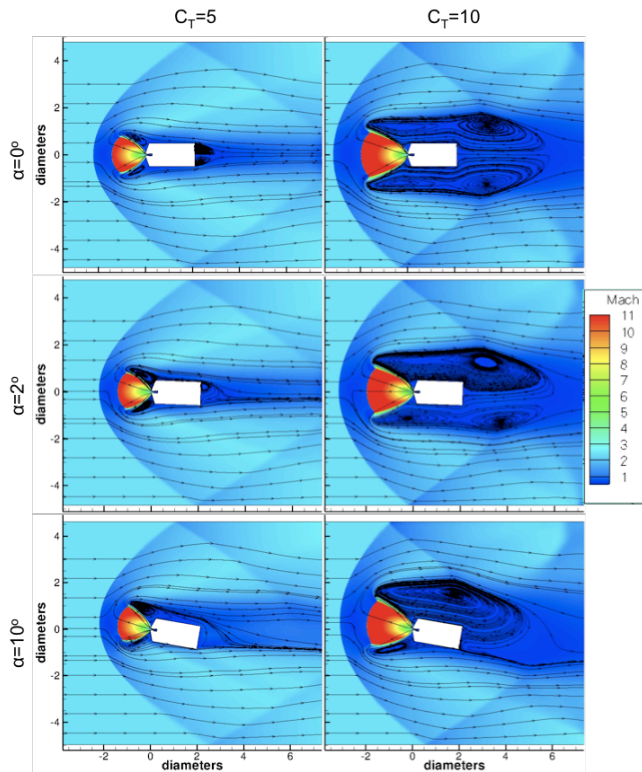


Figure 13: Flow field effects of angle-of-attack on single-nozzle configuration at $M=2.4$, $C_T=5$ and 10 . Only FUN3D is shown.

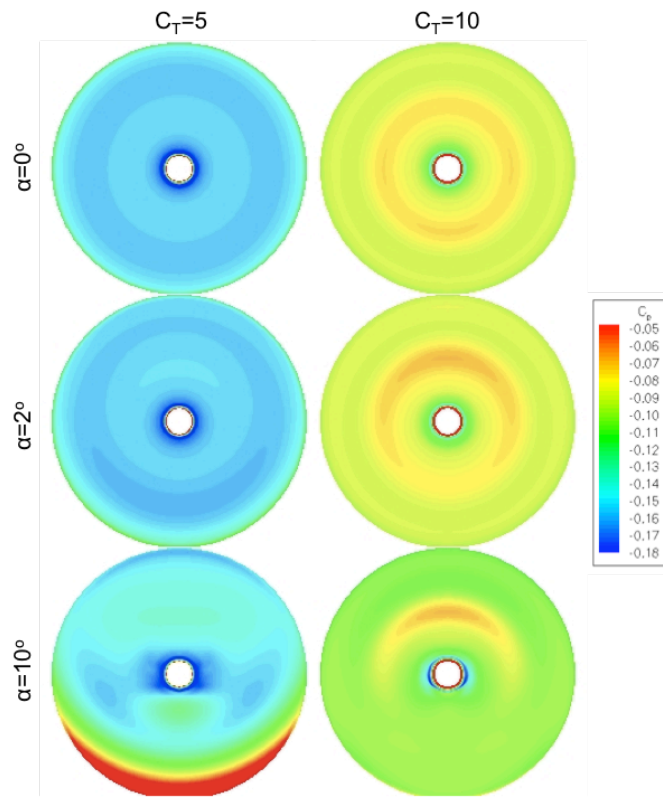


Figure 14: Pressure coefficient contour effects from angle-of-attack on single-nozzle configuration at $M=2.4$, $C_T=5$ and 10 . Only FUN3D is shown.

Three-Nozzle Configuration

This configuration has all three outer nozzles thrusting and the center nozzle plugged. The three-nozzle configuration analysis was only performed for zero angle-of-attack. Again the largest amount of tunnel interference is at $M=2.4$, $C_T=10$, $\alpha=0$ -degree. Here the Mach reflection off the wall occurs at the same diameter location as the model forebody (Figure 15). The tunnel blockage for the three-nozzle configuration at this thrust coefficient is not as severe as the single-nozzle configuration.

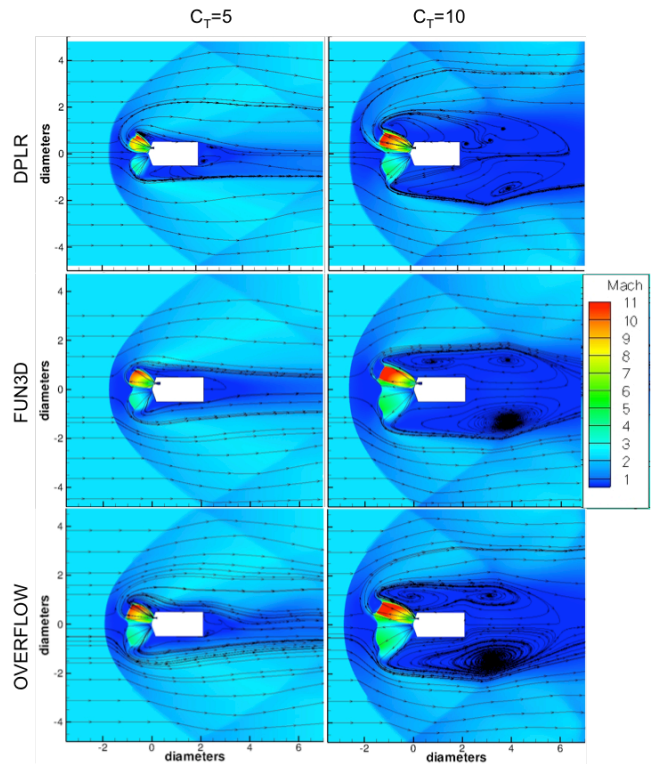


Figure 15: Flow field of three-nozzle configuration at $M=2.4$, $C_T=5$ and 10 at zero angle-of-attack for DPLR (top), FUN3D (middle), and OVERFLOW (bottom).

The three codes agree somewhat in locations of bow shock, interface and termination shock (Table 2). The maximum percent difference in bow shock location is 25% for $M=4.6$, $C_T=10$. DPLR and FUN3D predicted steady flow on this configuration. OVERFLOW is unsteady at all cases except for $M=2.4$, $C_T=10$. Slices taken at $\phi=0$ -degree and $\phi=90$ -degree (Figure 16) of the pressure coefficients, however, differ greatly at the nose as seen in Figure 17. The DPLR solution predicts significantly lower pressure coefficient on the nose. This discrepancy is currently being investigated and may be a result of the grid topology. The rise in pressure coefficient leading up to the nose is in accordance with FUN3D and OVERFLOW, and then there is a sharp decline in the region of the nose that has a unique grid topology (Figure 18). This is not seen in the single or four-nozzle configurations because this location is not modeled as a wall but rather a nozzle exit. The difference at the nose between FUN3D and OVERFLOW is about 30%. The outer

flank region of the model is at a nearly constant pressure coefficient for all three codes. The spike in pressure coefficient at the non-dimensional radial location of 0.5 is the location of the nozzle through slice $\phi=0$ -degree.

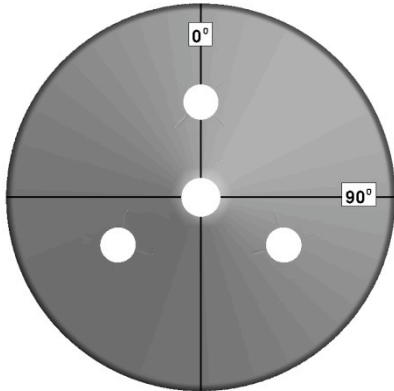


Figure 16: Location of pressure coefficient slices (at $\phi=0$ -degree and $\phi=90$ -degree) relative to the nozzles. Shown on the four-nozzle configuration model.

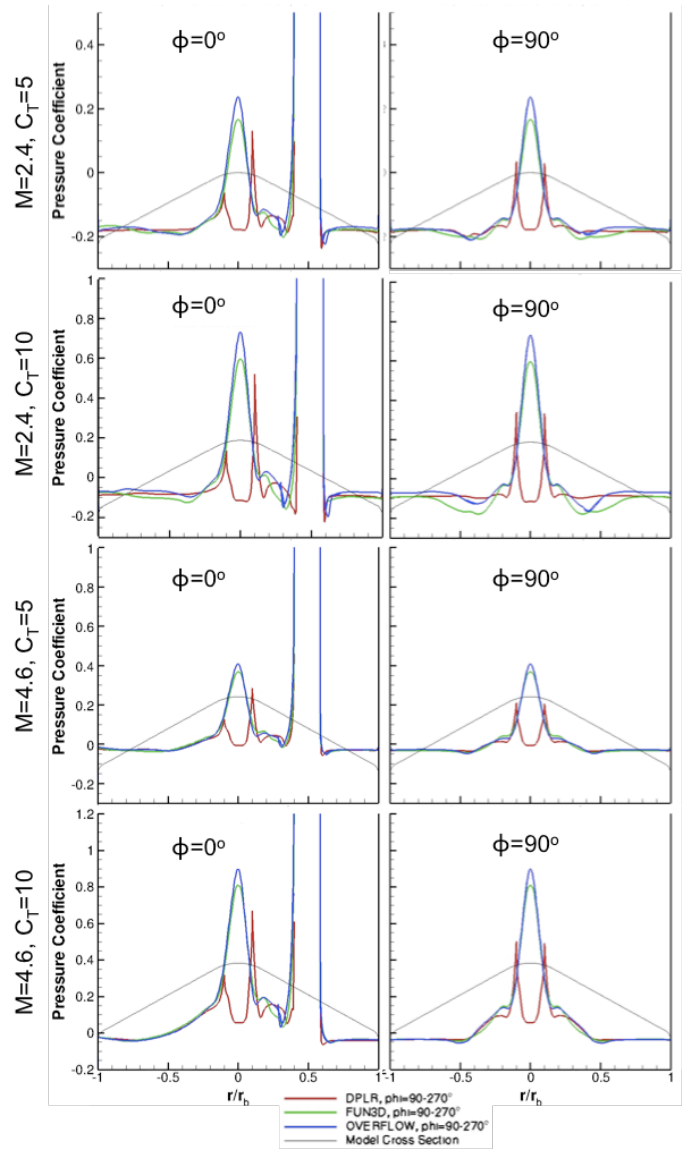


Figure 17: Pressure coefficient slices for three-nozzle configuration model at zero angle-of-attack for DPLR (red), FUN3D (green), and OVERFLOW (blue).

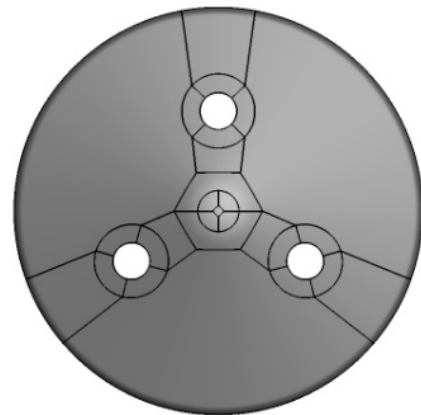


Figure 18: DPLR grid topology for the three-nozzle configuration.

Nozzles	Case		Slice Location	Bow Shock			Max % Difference	Termination Shock			Max % Difference
	Mach	CT		DPLR	FUN3D	OVERFLOW		DPLR	FUN3D	OVERFLOW	
1	2.4	5	Center Nozzle	2.33	2.23	2.31	4.48	1.40	1.39	1.41	1.44
		10		3.44	3.14	3.24	9.55	1.98	1.93	1.96	2.59
	4.6	5		2.13	2.15	2.16	1.41	1.34	1.46	1.45	8.96
		10		3.04	2.98	2.97	2.36	2.01	2.07	2.02	2.99
3	2.4	5	Peripheral Nozzle	1.82	1.60	1.78	13.75	0.97	0.87	0.87	11.49
		10		2.82	2.51	2.70	12.35	1.42	1.27	1.35	11.81
	4.6	5		1.84	1.56	1.67	17.95	1.02	0.90	0.92	13.33
		10		2.80	2.24	2.34	25.00	1.50	1.33	1.29	16.28
4	2.4	5	Center Nozzle	3.50	3.04	3.11	15.13	1.85	1.66	1.75	11.45
		10		8.21	3.96	7.75	107.32	3.88	2.38	3.90	63.87
	4.6	5		3.64	3.73	4.41	21.15	2.22	2.35	2.57	15.77
		10		5.72	5.78	6.28	9.79	3.48	3.68	3.87	11.21
4	2.4	5	Peripheral Nozzle	3.31	2.24	2.9	47.77	1.17	0.78	1.28	64.10
		10		7.60	3.35	6.76	126.87	1.57	1.64	1.37	19.71
	4.6	5		3.16	2.82	3.03	12.06	1.15	1.07	1.10	7.48
		10		4.78	4.26	4.49	12.21	1.70	1.44	1.55	18.06

Table 2: Bow and termination shock standoff distances with percent difference for all nozzle configurations, thrust coefficients and CFD codes.

Four-Nozzle Configuration

The shock standoff distances and interface locations vary much more in the four-nozzle configuration cases than in the cases with fewer nozzles (Table 2), particularly for Mach 2.4 (Figure 19). In the $M=2.4$, $C_T=5$ case the plume shape is asymmetric. The bow shock location is similar between codes, but the plume structures are quite different. The OVERFLOW plume differs from DPLR and FUN3D. Upon further examination, an asymmetry in the OVERFLOW plume was found when comparing slices taken through each peripheral nozzle (Figure 21). The OVERFLOW slice at $\phi=240$ -degrees compares well with the shape of the DPLR and FUN3D solutions. The FUN3D solution was not able to determine asymmetry because it was run at a 180-degree revolution with a forced symmetry plane. DPLR was run at a 360-degree revolution and did not see the asymmetry. At $M=2.4$, $C_T=10$, both DPLR and OVERFLOW predict a candle flame plume shape where FUN3D contains a blunt termination shock. This results in a large difference in shock standoff distances and interface location. FUN3D predicts a bow shock location of about 4 diameters upstream where DPLR and OVERFLOW are nearly twice that. At $M=4.6$ (Figure 20) agreement between the codes becomes much better, particularly at $C_T=10$. All three CFD codes predicted steady flow here. The presence of the center nozzle seems to attribute to the steadiness.

The effect of angle-of-attack on the flow field of $M=4.6$, $C_T=5$ is shown in Figure 22. At angle-of-attack the bow shock is no longer symmetric. A blunted edge forms on the bow shock, most evident in the $\alpha=10^\circ$ case. As the angle-of-attack increases the effective body diameter created by the plumes increases and pushes the bow shock out further.

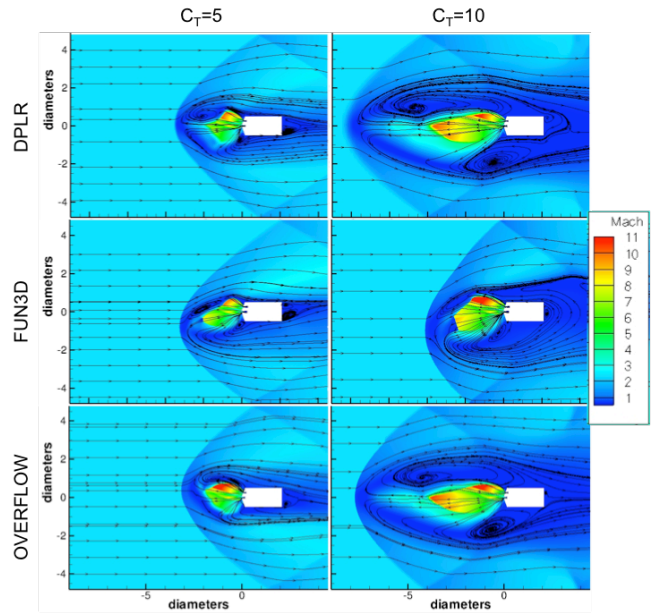


Figure 19: Four-nozzle configuration flow field at zero angle-of-attack at $M=2.4$, $C_T=5$ and 10 for DPLR (top), FUN3D (middle), and OVERFLOW (bottom).

5. SUMMARY

A SRP wind tunnel experiment was designed to provide high-fidelity data for CFD validation exercises in order to demonstrate modeling strengths and weaknesses. The experiment was designed to address current dataset limitations, particularly in the area of data uncertainties and flow conditions reporting. The CFD aided the model design process by indicating the potential for tunnel blockage or “unstart” with a 6-inch diameter model at $M=2.4$ and $C_T=10$. This result led to the final chosen diameter of 5 inches. CFD raised concerns about the issue of liquefaction within the plume and led to steps to minimize the likelihood of this occurring, such as heating the plenum and reducing the nozzle area ratio. The modeling of the internal manifolds suggested that separation would occur at the fingers of the nozzles. This resulted in the requirement to radius the corners at that location.

A pre-test CFD case matrix was designed for the desired Mach number range (2.4, 3.5, and 4.6), angle-of-attack range (0, 2, and 10 degrees) and thrust coefficient range (0, 5 and 10) with the final 5-inch model diameter. The matrix was calculated with three CFD codes (DPLR, FUN3D and OVERFLOW). The pre-test CFD analysis served as both a predictor for the wind tunnel test at the Langley UPWT and a code-to-code comparison, another step in CFD verification.

All three codes predict similar flowfield structures such as jet termination shock, interface, bow shocks and recirculation regions. However, the codes differ on the level of unsteadiness predicted. DPLR tends to predict a low level of oscillation at the triple point whereas FUN3D is steady for every case and OVERFLOW exhibits steadiness for some cases.

The FUN3D and OVERFLOW codes agree well between each other for the current set of cases. Although all three codes used the SST turbulence model, each had a slightly different version of the model. The DPLR SST model is vorticity based while FUN3D and OVERFLOW SST models are strain based. Further work should investigate other turbulence models or improvements to current models needed specifically for SRP.

Once data from the Langley UPWT test are made available, a post-test CFD study will commence. This future study for SRP CFD will include a thorough grid sensitivity study. With shocks and shear layers being present in the plume structure, care needs to be taken to assure the proper physics are being represented with an adequate level of grid refinement. A time resolution study will also be performed because of the large amount of high-frequency measurements taken during the test.

Future wind tunnel tests will be designed to provide additional data for CFD validation and will build upon the experience in the Langley facility. Among the desired data products are integrated force and moment measurements on more realistic configurations and interference aeroheating data.

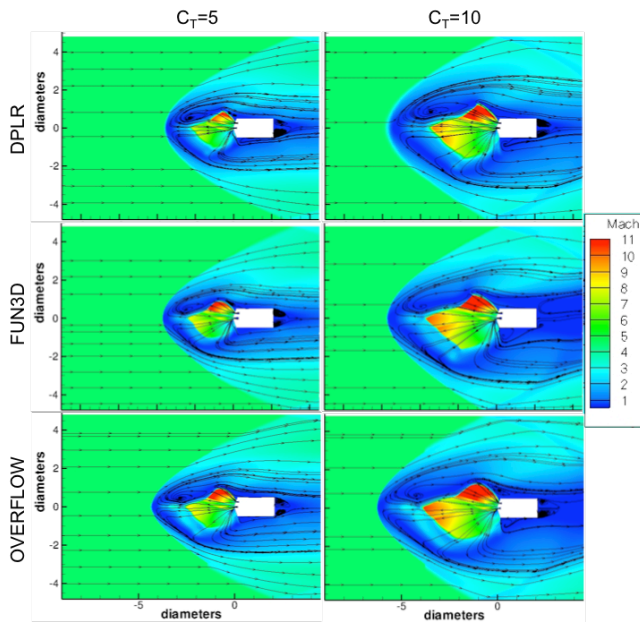


Figure 20: Four-nozzle configuration flow field at zero angle-of-attack at $M=4.6$, $C_T=5$ and 10 for DPLR (top), FUN3D (middle), and OVERFLOW (bottom).

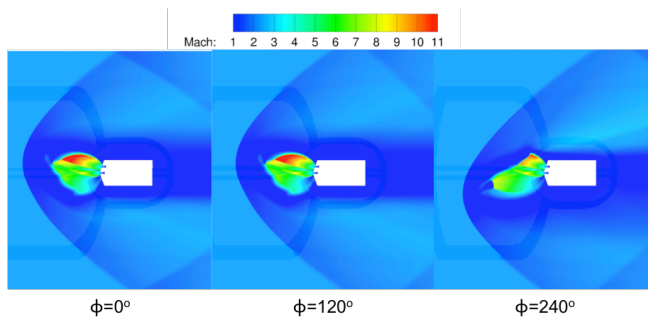


Figure 21: Asymmetry in plume shown at slices through each peripheral nozzle for $M=2.4$, $C_T=5$ in OVERFLOW.

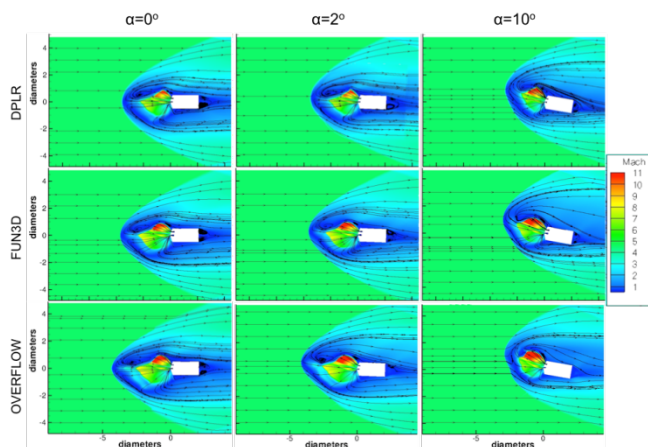


Figure 22: Four-nozzle configuration flow field at angle-of-attack at $M=4.6$, $C_T=5$ for DPLR (top), FUN3D (middle), and OVERFLOW (bottom).

ACKNOWLEDGEMENTS

The first author would like to thank Michael Barnhardt and Todd White for support on DPLR best practices and Andrew J. Hyatt for overset gridding assistance. The second author would like to thank Pieter Buning, Phil Stuart, Tom Booth, and Darby Vicker for valuable guidance on gridding and solver best practices. The third author would also like to thank William T. Jones of NASA Langley Research Center, Hampton, VA for enabling very rapid unstructured grid generation thanks to his GridEx/batchEx software. Time from geometry to grid was typically less than a day and even then the lion's share was due to serial volume grid generation and not user interaction.

REFERENCES

- [1] Zang, T. A., "Entry, Descent and Landing Systems Analysis Study: Phase 1 Report," EDL Systems Analysis Team, NASA TM-2010-0000002009, May 2010.
- [2] Edquist, K.T., Dyakonov, A.A., Shidner, J.D., Studak, J.W., Tigges, M.A., Kipp, D.M., Prakash, R., Trumble, K.A., Dupzyk, I.C., Korzun, A.M., "Development of Supersonic Retro-Propulsion for Future Mars Entry, Descent, and Landing Systems," AIAA-2010-5046, June 2010.
- [3] Korzun, A.M., Braun, R.D., and Cruz, J.R., "Survey of Supersonic Retropropulsion Technology for Mars Entry, Descent, and Landing," *Journal of Spacecraft and Rockets*, Vol. 46, No. 5, September-October 2009.
- [4] Trumble, K.A., Schauerhamer, D.G., Kleb, W.L., Carlson, J-R., Buning, P.G., Edquist, K.T., Barnhardt, M.D., "An Initial Assessment of Navier-Stokes Codes Applied to Supersonic Retro-Propulsion," AIAA-2010-5047, June 2010.
- [5] Wright, M.W., White, T., and Mangini, N., "Data Parallel Line Relaxation (DPLR) Code User Manual Acadia – Version 4.01.1," NASA/TM-2009-215388, October 2009.
- [6] Anderson, W.K. and Bonhaus, D.L., "An Implicit Upwind Algorithm for Computing Turbulent Flows on Unstructured Grids," *Journal of Computational Physics*, Vol. 128, No. 2, 1996, pp. 391-408.
- [7] Anderson, W. K., Rausch, R. D., and Bonhaus, D. L., "Implicit/Multigrid Algorithm for Incompressible Turbulent Flows on Unstructured Grids," *Journal of Computational Physics*, Vol. 128, No. 2, 1996, pp. 391–408.
- [8] Buning, P. G., Jespersen, D. C., Pulliam, T. H., Klopfer, G. H., Chan, W. M., Slotnick, J. P., Krist, S. E., and Renze, K. J., "Overflow User's Manual," NASA Langley Research Center, Hampton, VA, 2002.
- [9] Jarvinen, P.O. and Adams, R.H., "The Aerodynamic Characteristics of Large Angled Cones with Retrorockets," NASA Contract No. NAS7-576, Cambridge, MA, Feb. 1970.
- [10] Berry, S.A., Laws, C.T., Kleb, W.L., Rhode, M.N., Spells, C., Mccrea, A.C., Trumble, K.A., Schauerhamer, D.G., Oberkampf, W.L., "Supersonic Retro-Propulsion Experimental Design for Computational Fluid Dynamics Model Validation," IEEE Aerospace Conference Paper No. 1499, March 2011.
- [11] MacCormack, R.W. and Candler, G.V., "The Solution of the Navier-Stokes Equations Using Gauss-Seidel Line Relaxation," *Computers and Fluids*, Vol. 17, No. 1, 1989, pp. 135-150.
- [12] Yee, H.C., "A Class of High-Resolution Explicit and Implicit Shock Capturing Methods," NASA TM 101088, Feb. 1989.
- [13] Edwards, J. R., "A Low-Diffusion Flux-Splitting Scheme for Navier-Stokes Calculations," *Computers & Fluids*, Vol. 26, 1997, pp. 653-659.
- [14] Menter, F. R., "Two-Equation Eddy-Viscosity Turbulence Models for Engineering Applications," *AIAA Journal*, Vol. 32, No. 8, 1994, pp. 1598– 1605.
- [15] Park, M. A., "Anisotropic Output-Based Adaptation with Tetrahedral Cut Cells for Compressible Flows," Ph.D. thesis, Massachusetts Institute of Technology, Sept. 2008.
- [16] Park, M. A. and Darmofal, D., "Parallel Anisotropic Tetrahedral Adaptation," AIAA Paper 2008–917, 2008.
- [17] Benek, J. A., Buning, P. G., and Steger, J. L., "A 3-D Chimera Grid Embedding Technique," AIAA Paper 85-1523, 1985.
- [18] Chan, W.M., Gomez III, R.J., Rogers, S.E., and Buning, P.G., "Best Practices in Overset Grid Generation," AIAA-2002-3191, June 2002.
- [19] Jespersen, D.C., Pulliam, T.H., and Buning, P.G., "Recent Enhancements to OVERFLOW (Navier-Stokes Code)," AIAA-97-0644, Jan. 1997.
- [20] Tramel, R., Nichols, R., and Buning, P.G., "Addition of Improved Shock-Capturing Schemes to OVERFLOW 2.1," AIAA-2009-3988, 19th AIAA Computational Fluid Dynamics, San Antonio, Texas, June 22-25, 2009.
- [21] Pulliam, T.H., and Chaussee, D.S., "A Diagonalized Form of an Implicit Approximate Factorization Algorithm," *J. Comp. Physics*, Vol. 39, 1981.

[22] Nichols, R., Tramel, R., and Buning, P., "Solver and Turbulence Model Upgrades to OVERFLOW 2 for Unsteady and High-Speed Applications," AIAA-2006-2824, June 2006.

[23] Pandya, S.A., Venkateswaran, S., and Pulliam, T.H., "Implementation of Preconditioned Dual-Time Procedures in OVERFLOW", AIAA-2003-0072, Jan. 2003.

[24] Baldwin, B.S., and Barth, T.J., "A One-Equation Turbulence Transport Model for High Reynolds Number Wall-Bounded Flows," AIAA-91-0610, Jan. 1991.

[25] Spalart, P.R., and Allmaras, S.R., "A One-Equation Turbulence Model for Aerodynamic Flows," AIAA-92-0439, Jan. 1992.

[26] Menter, F. R., "Two-Equation Eddy-Viscosity Turbulence Models for Engineering Applications," AIAA Journal, Vol. 32, No. 8, 1994, pp. 1598– 1605.

[27] Meakin, R.L., "Object X-Rays for Cutting Holes in Composite Overset Structured Grids," AIAA-2001-2537, June 2001.

[28] Jespersen, D.C., "Parallelism and OVERFLOW," NAS Technical Report NAS-98-013, NASA Ames Research Center, Moffett Field, CA, Oct. 1998.

[29] Meakin, R.L., "Automatic Off-Body Grid Generation for Domains of Arbitrary Size," AIAA-2001-2536, June 2001.

[30] Meakin, R.L., "An Efficient Means of Adaptive Refinement within Systems of Overset Grids," AIAA-95-1722, June 1995.

[31] Murman, S., Chan, W.M., Aftosmis, M.J., and Meakin, R.L., "An Interface for Specifying Rigid-Body Motions for CFD Applications", AIAA-2003-1237, Jan. 2003.

[32] Meakin, R.L., "Multiple-Body Proximate-Flight Simulation Methods," AIAA-2005-4621, June 2005.

BIOGRAPHY

Kerry Trumble is an aerospace engineer in the Aerothermodynamics Branch at the NASA Ames Research Center. Her primary focus is in the field of hypersonic computational fluid dynamics, in which she has been involved in the aerothermal analysis of Stardust, Orion Crew Exploration Vehicle, Space Shuttle Damage Assessment and Supersonic Retro-Propulsion. She received her B.S. in Mechanical Engineering from Michigan Technological University and her M.S. in Aerospace

Engineering from University of Minnesota, where her thesis was on flow control through laser energy deposition.

Guy Schauerhamer is an aerospace engineer for Jacobs Technology supporting NASA Johnson Space Center's Applied Aeroscience and CFD Branch. He received his B.S. and M.S. in Mechanical Engineering from Utah State University where his thesis was on six-degree-of-freedom moving mesh applications. His primary focus is in the field of computational fluid dynamics, in which he has been involved in the aerodynamic analysis of Mars entry capsules, sounding rockets, Ares V, various Space Shuttle aspects, and supersonic retro-propulsion.

Bil Kleb is an aerospace engineer in the Aerothermodynamics Branch at the NASA Langley Research Center. His main area of research has been the development and application of hypersonic computational fluid dynamics codes such as LAURA and FUN3D. He has a long history of providing aerothermodynamic analysis of the shuttle and has contributed to numerous NASA space access studies such as X-33, X-34, X-37, and Orion. His current research focuses on verification and validation of computational fluid dynamic models to enable prediction of Mars decelerator reentry performance. He has a B.S. and M.S. in Aeronautics and Astronautics from Purdue University, an M.B.A. from the College of William and Mary, and a Ph.D. in Aerospace Engineering from the University of Michigan.

Jan-Renee Carlson is an aerospace engineer in the Computational Aero-Sciences Branch at the NASA Langley Research Center. She started at the 16-Foot Transonic Tunnel as a wind tunnel engineer in 1980. Her main area of research has been the development and application of the computational fluid dynamics code FUN3D for air-breathing propulsion simulations. Her current research focuses on in-code solution visualization, turbulence modeling and validation of computational fluid dynamic models to enable prediction of subsonic and supersonic propulsion-airframe aerodynamics. She has a B.S. and M.S. in Physics from Clarkson University and a M.S. in Mechanical Engineering from George Washington University.

Karl Edquist is an Aerospace Engineer in the Atmospheric Flight and Entry Systems Branch at the NASA Langley Research Center in Hampton, Virginia. His areas of expertise are computational aerothermodynamics and aerodynamics, and he has authored or co-authored several papers in these fields. He currently is the Supersonic Retropropulsion Lead for the Entry, Descent, and Landing Project. He also serves as the Aerothermal Lead for the Mars Science Laboratory entry capsule. He received his B.S. in Aerospace Engineering from the University of Colorado and M.S. in Aerospace Engineering from the University of Maryland.